Filaments in the edge confinement region of TJ-II

B.Ph. van Milligen[1], J.H. Nicolau[2], B. Liu[3], G. Grenfell[4], U. Losada[1], B.A. Carreras[2], L. García[2], C. Hidalgo[1] and the TJ-II Team

[1] CIEMAT - Laboratorio Nacional de Fusión, Avda. Complutense 40, 28040 Madrid, Spain
[2] Universidad Carlos III, 28911 Leganés, Madrid, Spain
[3] Institute of Fusion Science, School of Physical Science and Technology, Southwest Jiaotong University, Chengdu, China
[4] Universidade de São Paulo, Instituto de Física, São Paulo, Brazil

Abstract. Floating potential measurements taken in the edge region of the plasma of the TJ-II stellarator are analyzed. Data from two remote reciprocating probes are analyzed using the Transfer Entropy, revealing the spatial dimensions and propagation of filamentary structures. The Transfer Entropy allows distinguishing contributions to Long Range Correlations from Zonal Flows and filaments. The results are corroborated by performing simulations with a resistive MHD model and analyzing data from synthetic diagnostics.

1. Introduction

Due to the magnetic field structure of magnetically confined plasmas, plasma turbulence vortices have a filamentary structure. The toroidal magnetic flux surfaces are characterized by a rotational transform of $\iota = \iota/2\pi = 1/q = n/m$, where q is the safety factor and n/m indicates the number of toroidal per poloidal windings of the field lines. The filaments are typically associated with magnetic surfaces that are characterized by low values of m and n. They have a small radial extension, while their poloidal extension is given by $\pi r/m$, but they extend long distances in the toroidal direction (along the magnetic field lines), forming filamentary toroidal knots. These topological structures can be visualized by representing the volume where the plasma potential Φ exceeds a threshold value [1]. These structures may be the origin of the filaments observed in the SOL, often referred to as 'blobs' [2].

The present study focuses on the detection of the structure of the plasma potential in the confinement region using a diagnostic set up and an analysis approach that allows us to determine their limited poloidal extension, radial width and large toroidal size. At the same time, we can measure the poloidal rotation of the plasma at the filament position.

In TJ-II, filaments have been observed indirectly using soft X-ray measurements [3] and visualized using fast cameras in the edge region [4, 5]. Similarly, filaments in the edge region of the W7-X stellarator were also visualized recently [6].

In previous work, we have used TJ-II's double reciprocating Langmuir probe system to determine the approximate shape of filaments in the edge region. This was done by performing scans of the rotational transform within a discharge, while the Langmuir probes were inserted at a fixed radial position inside the plasma, and determining the (long range) correlation between the two probes at remote locations. The filamentary structure could then be deduced using a simple model for the expected correlation produced by filaments [7]. Thus, we found that the size of the filamentary structures along the field lines is $L_{||} \simeq 40 - 50$ m (implying 4 to 5 toroidal turns), whereas the (poloidal) extension of the structures perpendicular to the field lines is $L_{\perp} \simeq 7$ cm.

In the present work, we use a relatively new technique (the Transfer Entropy [8]) to analyze data from the same reciprocating Langmuir probes. This time, we use a fixed magnetic configuration but apply voltage to a biasing probe in order to modify the radial electric field, E_r, in the edge region, i.e., we vary the poloidal rotation of the edge plasma by imposing an additional $E \times B$ flow, $v_\theta = E_r/B_\phi$. Filaments are detected when the poloidal rotation causes a filament to cross both toroidally distant probe locations successively.

We use a resistive Magneto-Hydrodynamic model to reproduce and support some of the experimental observations shown. For this purpose, synthetic probes are defined and analyzed using similar methods as those applied to the measurements at TJ-II. The analysis reveals information about the poloidal periodicity, the poloidal velocity and radial width of these filamentary structures.

This paper is structured as follows. In Section 2, the experimental setup is discussed. In Section 3, we present the experimental results. In Section 4, we present the modeling results. In Section 5, we discuss the results, and draw some conclusions.

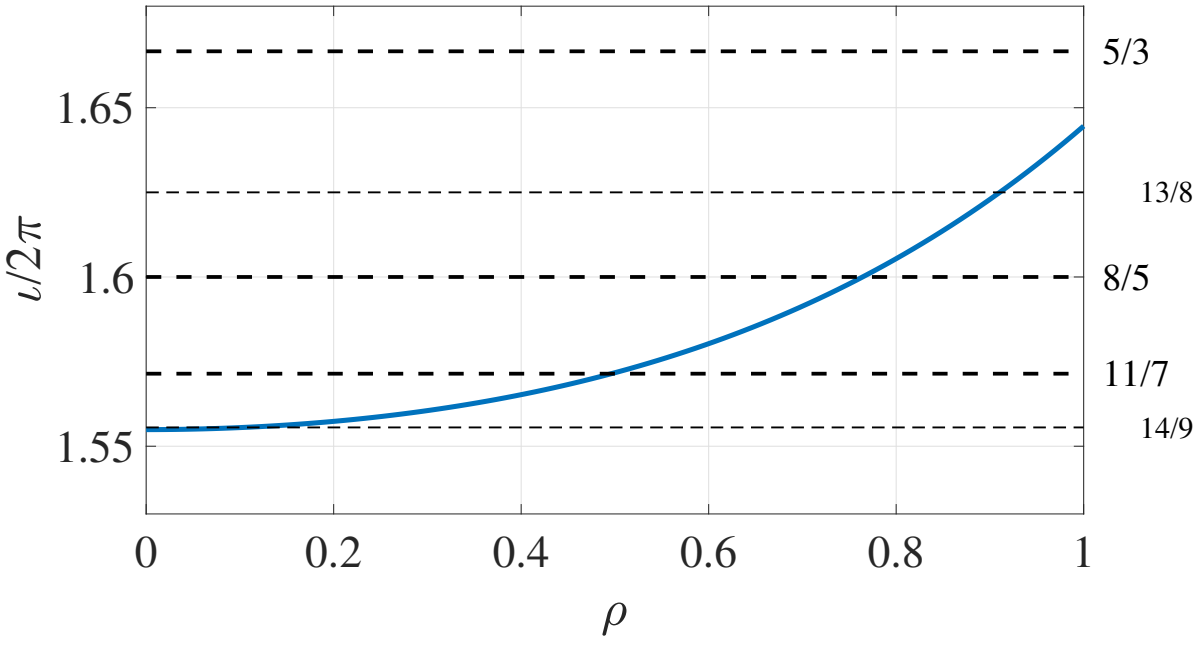

Figure 1. ι profile for the standard magnetic configuration (100_44_64). Some rational values are indicated by horizontal dashed lines.

2. Experimental set-up and techniques used

The experiments reported here were performed in the 4-period TJ-II stellarator (magnetic field $B_T \simeq 1$ T, major radius $R_0 = 1.5$ m, minor radius $\langle a \rangle \leq 0.22$ m). The magnetic configuration used is the 'standard' configuration (labelled 100_44_64), which has the rotational transform profile (ι) shown in Fig. 1. Discharges were initiated by Electron Cyclotron Resonant Heating (ECRH; $P_{ECRH} \leq 400$ kW), followed by a Neutral Beam Injection (NBI) heated phase (port-through $P_{\rm NBI} \simeq 450$ kW). In the ECRH phase, the line average electron density was low ($\overline{n}_e \simeq 0.3 - 0.5 \cdot 10^{19}$ m^{-3}), but in the NBI phase, densities of up to about $\overline{n}_e \simeq 6 \cdot 10^{19}$ m^{-3} were reached.

2.1. Biasing electrode and Langmuir probes

A graphite electrode was installed on a reciprocating probe drive at Sector A8 ($\phi = 174.4°$) and biased with respect to a radially movable limiter at sector C3 ($\phi = 298.1°$). In the present experiments the electrode was inserted 3 cm into the plasma, corresponding to $\rho = r/a \sim 0.85$ inside the Last Closed Flux Surface (LCFS), whereas the limiter was kept at the LCFS ($\rho = 1$).

The electrode was biased with respect to the limiter with an AC voltage during plasma discharges. The waveform of the biasing voltage was a negative half-wave rectified triangular wave, i.e. in each period, one unbiased half-cycle with $V_{\rm bias} = 0$ and one biased half-cycle with a triangular shape peaked at $V_{\rm bias} = -340$ V, in order to allow a comparison between the unbiased and biased state in a single discharge. The

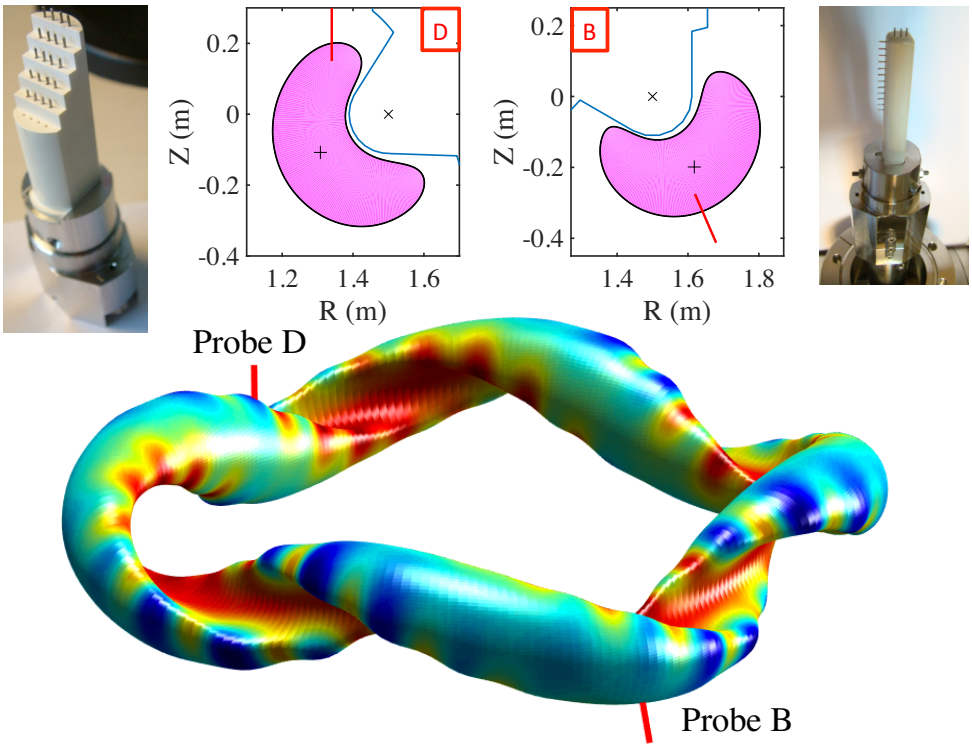

Figure 2. Schematic of reciprocating Langmuir probe locations in TJ-II. The top diagrams show poloidal cross sections at the toroidal angles of the two probes, and includes the probe trajectories (red), the last closed flux surface (black outline), the magnetic axis (+), the location of the machine core ($R_0 = 1.5$ m, $Z = 0$, indicated by a ×) and part of the vacuum vessel (blue line). The bottom 3-D figure shows the last closed flux surface (where colors represent the magnetic field strength) and the probe trajectories as red lines.

frequency of the biasing waveform was varied and frequencies of 40, 60 and 80 Hz were chosen for the present experiments.

Measurements were performed using two reciprocating Langmuir probe arrays, located in Sectors D ($\phi = 38.2°$) and B ($\phi = 195°$), as indicated schematically in Fig. 2. Probe D is a two-dimensional probe array with 44 tips, spaced radially by 5 mm and poloidally by 3 mm. The first and third column of tips was set to measure the floating potential, whereas the second column was set to measure the ion saturation current, $I_{\rm sat}$. Probe B is a rake probe consisting of eight tips, spaced radially by 2.3 mm. All tips on Probe B were configured to measure floating potentials. This setup allows measuring plasma fluctuations simultaneously at two poloidally / toroidally distant locations.

2.2. Transfer Entropy

In this work, we use a technique from the field of Information Theory [8] that was recently applied for the first time in the context of fusion plasmas [9]: the Transfer Entropy. This nonlinear technique measures the 'information transfer' between two signals, is directional, and uses all the information available in the two signals, regardless of amplitude or sign.

The Transfer Entropy is a measure of the causal relation or information flow between two time series. The Transfer Entropy between discretely sampled signals $y(t_i)$ and $x(t_i)$ quantifies the number of bits by which the prediction of the next sample of signal x can be improved by using the time history of not only the signal x itself, but also that of signal y.

In this work, we use a simplified version of the Transfer Entropy:

$$T_{Y\to X} = \sum p(x_{n+1}, x_{n-k}, y_{n-k}) \log_2 \frac{p(x_{n+1}|x_{n-k}, y_{n-k})}{p(x_{n+1}|x_{n-k})}. \quad (1)$$

Here, $p(a|b)$ is the probability distribution of a conditional on b, $p(a|b) = p(a,b)/p(b)$. The probability distributions $p(a, b, c, \ldots)$ are constructed using m bins for each argument, i.e., the object $p(a, b, c, \ldots)$ has m^d bins, where d is the dimension (number of arguments) of p. The sum in Eq. 1 runs over the corresponding discrete bins. The number k can be converted to a 'time lag' by multiplying it by the sampling rate. The construction of the probability distributions is done using 'course graining', i.e., a low number of bins (here, $m = 3$), to obtain statistically significant results. For more information on the technique, please refer to Ref. [9]. The value of the Transfer Entropy T, expressed in bits, can be compared with the total bit range, $\log_2 m$, equal to the maximum possible value of T, to help decide whether the Transfer Entropy is significant or not.

The statistical significance of the Transfer Entropy can be estimated by calculating T for two random (noise) signals [10]. Here, we will be analyzing time intervals with a typical duration of about 2 ms, corresponding to $N = 2 \cdot 10^3$ points, and the statistical significance level of T is of the order of $4 \cdot 10^{-3}$.

Regarding the interpretation of the Transfer Entropy, we note that it is a nonlinear quantifier of information transfer and helps clarifying which fluctuating variables influence which others - without specifying the nature of this influence. In this sense, it is fundamentally different from the cross correlation, which is maximal for two identical signals ($x = y$), whereas the Transfer Entropy is exactly zero for two identical signals (as no information is gained by using the second, identical signal to help predicting the behavior of the first). Furthermore, the Transfer Entropy is *directional* and therefore capable of distinguishing perturbations propagating from y to x or vice versa.

Finally, we note that the Transfer Entropy is a 'causality detection' technique, and therefore always and by definition involves a time delay. Thus, this technique is insensitive to simultaneously occurring events, such as those corresponding to floating potential variations on a flux surface produced by Zonal Flows (with poloidal and

toroidal symmetry) [11]. Consequently, Zonal Flows, if present and affecting the floating potential measurements we will be using here, are not detected by this technique.

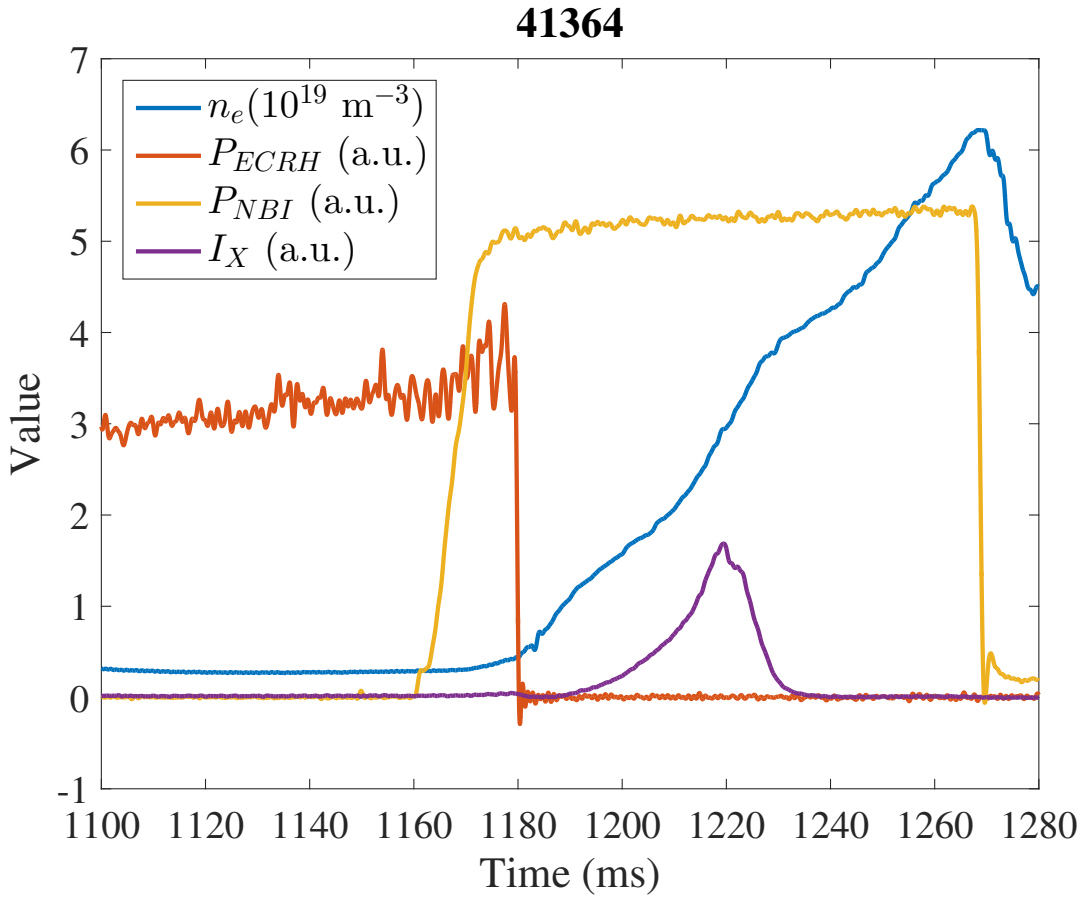

Figure 3. Some time traces for discharge 41364. I_X is the soft X-ray emission along a central viewing chord.

3. Experiments

3.1. Initial detection of rotating non-periodic structures in cold plasma

Fig. 3 shows some time traces indicating plasma evolution. Initially, the plasma is heated by ECRH, which is switched off at $t = 1180$ ms, while NBI1 is switched on at $t \simeq 1170$ ms. Density is low in the initial ECRH phase ($\overline{n_e} \simeq 0.3 \cdot 10^{19}$ m^{-3}), but rises steadily after the NBI is switched on, reaching a maximum value of about $\overline{n_e} \simeq 6 \cdot 10^{19}$ m^{-3} around $t \simeq 1270$ ms. This sequence of events also means that the plasma potential in the core transits from positive (in the ECRH phase) to negative (in the NBI phase) [12], so that the unbiased radial electric field in the edge region, E_r, is initially positive and turns negative later on.

Fig. 4 shows the floating potentials measured by two poloidally separated probe pins of probe D. Fig. 5 shows an example of the Transfer Entropy, calculated between two poloidally separated pins measuring V_f in probe D (top row) and between a pin of probe D and a pin of probe B (bottom row). During the initial part of the NBI phase ($1180 < t < 1220$ ms), with densities $\overline{n_e} \leq 3 \cdot 10^{19}$ m^{-3}, radiation is rapidly increasing

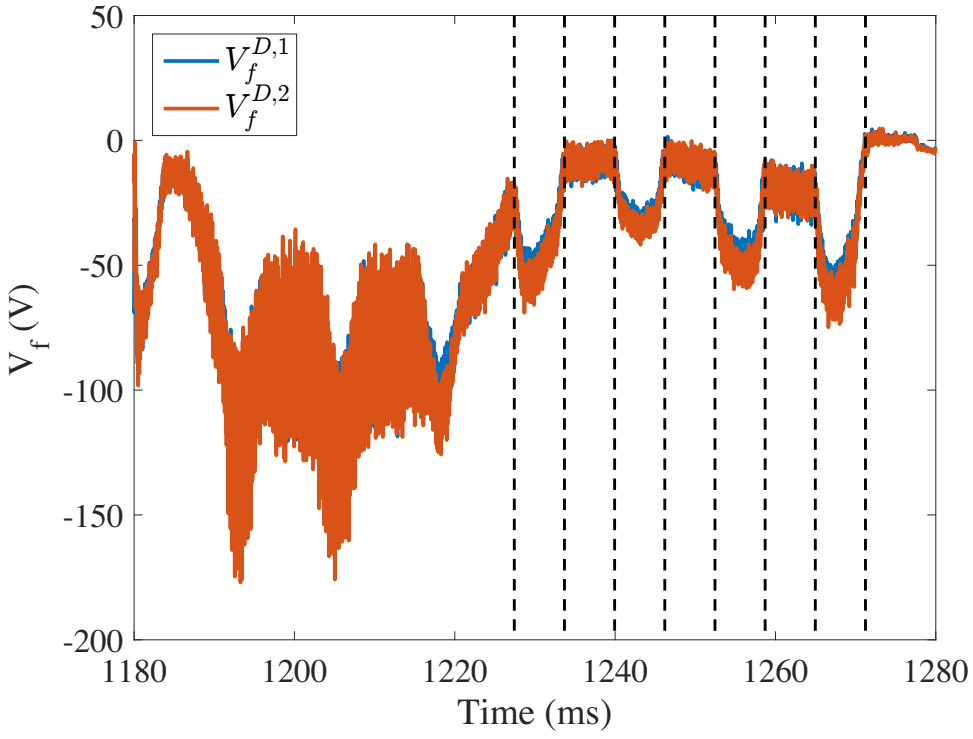

Figure 4. Floating potentials measured by two poloidally separated probe pins of probe D (discharge 41364). Vertical dashed lines indicate the start and end of modulation cycles.

and by the end of this phase, the plasma has radiated away most of its thermal energy. The value of the potential measured by the probes is indicative of the negative radial electric field, assuming it tends to zero near the LCFS. The V_f signals exhibit a high fluctuation level on top of the externally induced modulation, characteristic of plasma turbulence. The impact of high frequency Alfvén modes in this initial part of the NBI phase is clearly visible in the TE graph; the upward trend of the Alfvén period matches the upward evolution of the square root of the electron density, $\overline{n_e}$ (cf. Fig. 3), in accordance with expectation. After $t \simeq 1220$ ms, when the plasma is dense but cold, the mean absolute value of the plasma potential is reduced, and yet the impact of the modulation on the floating potential is very clear. The Transfer Entropy detects a clear and unidirectional time delay between the probe pins used, of the order of $2-3$ μs in the case of two poloidally separated pins of probe D, and of the order of $4-8$ μs in the case of two toroidally separated pins from probes D and B, matching the modulation cycles as time progresses.

Given the poloidal spacing of the probe pins (1 cm), a time delay of 3 μs would correspond to a poloidal rotation speed of about 3 km/s. The temporal shape of the Transfer Entropy maxima (a U shape) reflects the shape of the imposed modulation,

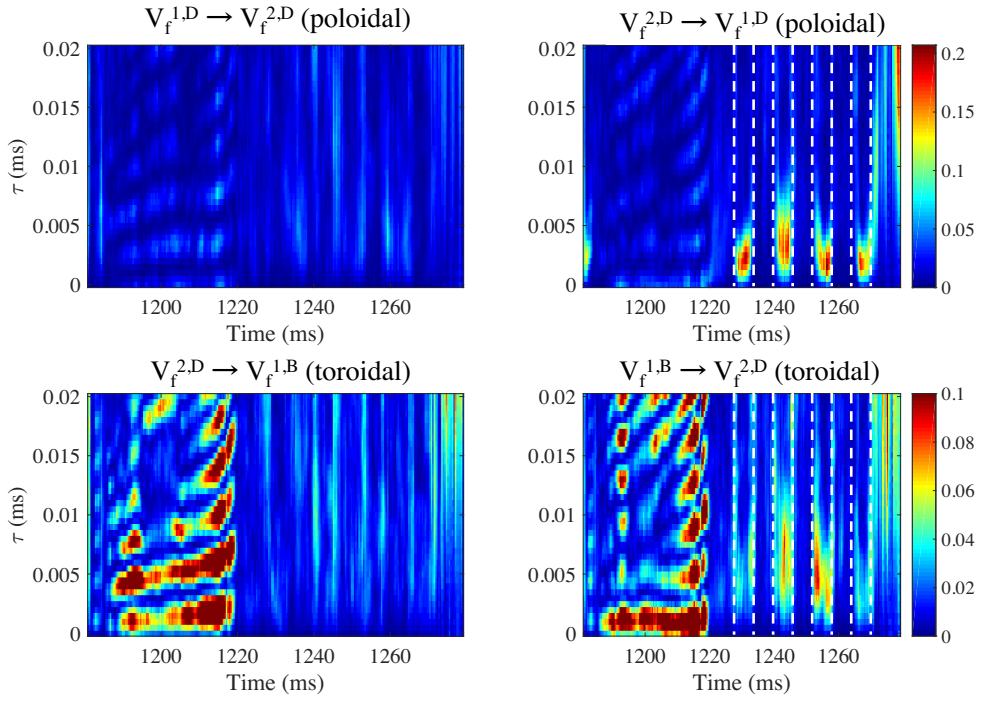

Figure 5. Transfer Entropy (discharge 41364. Top: TE between poloidally displaced probe pins. Bottom: TE between toroidally separated probe pins. Vertical dashed lines indicate the start and end of modulation cycles (cf. Fig. 4). Colors indicate the value of the TE, according to the scales shown on the right.

leaving no doubt that the observed time delays are the result of plasma rotation, imposed by modulation. Finally, each Transfer Entropy maximum at a given time $t > 1220$ ms is unique, very different from the Alfvén wave pattern seen for $t < 1220$ ms, which is repetitive along the vertical direction (time lag), as expected for a coherent mode. Thus, the TE maxima for $t > 1220$ ms (at lags below 8 μs) correspond to structures that rapidly decay in time (different from coherent modes), and we associate them with rotating turbulent filaments with a short lifetime. Below, we will explore the toroidal and radial size of these structures using the probe setup of TJ-II, which will confirm that these structures are filamentary.

Fig. 6 shows the standard cross correlation versus time (calculated using time intervals with a length of 1 ms) for comparison with the Transfer Entropy results. The basic pattern is rather similar as that obtained with the TE. The Alfvén wave appearing for $t < 1220$ ms is clearly seen using both methods. It should be noted that each TE maximum corresponds to either a correlation maximum or a minimum. During the periods when the modulation is active, the Transfer Entropy shows a very clear directionality. However, unlike the TE, the cross correlation does not drop to zero for $\Delta t = 0$ ms, making it somewhat difficult to deduce the rotation direction from the cross correlation alone, especially in the long-range correlated case. We ascribe this to

the existence of a Zonal Flow contribution, which by its nature (being a 'global' structure on a flux surface, i.e., $m = n = 0$) leads to simultaneous fluctuations (at $\Delta t = 0$) in the pins of probes B and D, separated by a long toroidal and poloidal distance. As noted above, the TE 'filters out' the Zonal Flow contribution, leading to a much clearer result regarding filament propagation and propagation direction.

Summarizing, both correlation and TE detect the filaments, but the correlation results are 'contaminated' with the Zonal Flow contribution. From a different point of view, comparing TE and correlation results might allow identifying the Zonal Flow contribution.

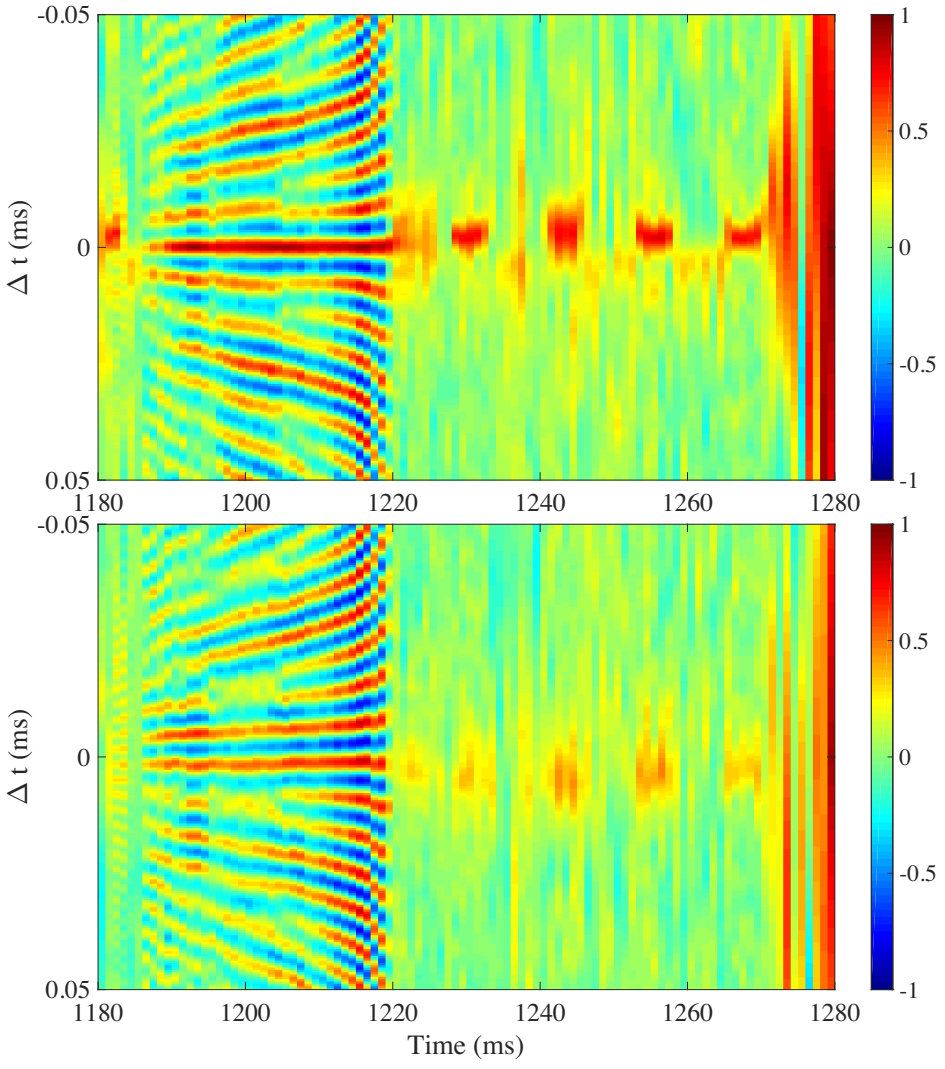

Figure 6. Cross correlation between the same probe pins as shown in Fig. 5. Top: poloidally displaced pins (of probe D). Bottom: toroidally displaced pins (of probes D and B).

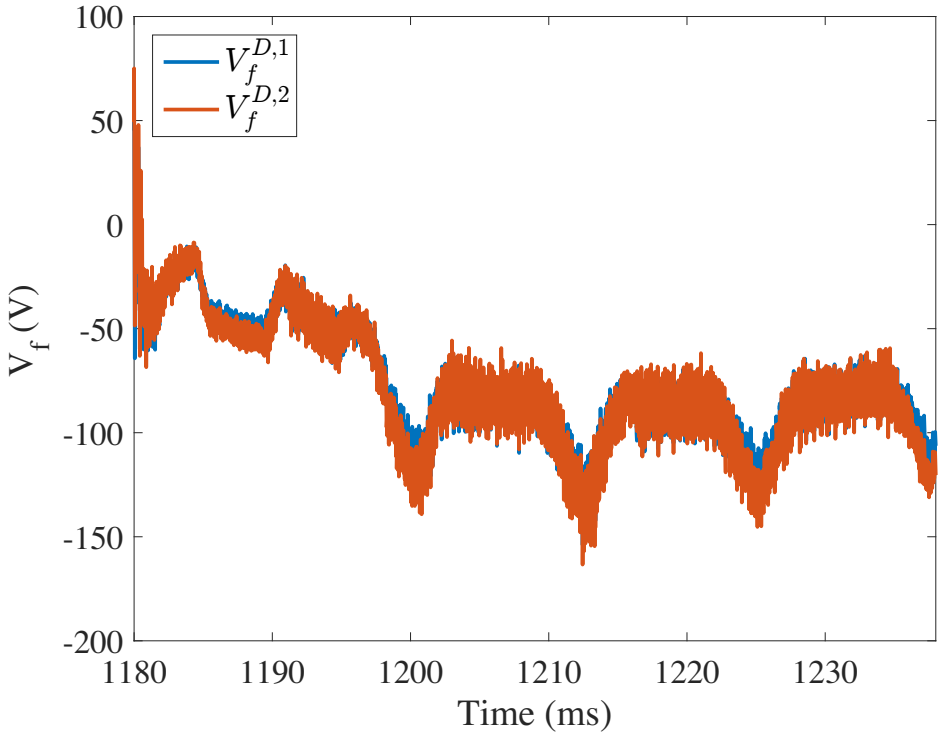

Figure 7. Floating potentials measured by two poloidally separated probe pins of probe D (discharge 41373).

3.2. Detection of rotating non-periodic structures in hot plasma

Fig. 7 shows time traces of the V_f measurements of two poloidally separated probe pins (probe D). As in the previous case, this corresponds to the NBI phase of the discharge, with mean negative floating potential (i.e., mean negative E_r in the edge region). In this case, there is no radiative collapse and the plasma continues hot (with gradually rising density from $\overline{n_e} \simeq 0.6$ to about $2.8 \cdot 10^{19}$ m^{-3} in the time window shown). The externally imposed modulation is clearly visible in the V_f time traces.

Fig. 8 shows the Transfer Entropy calculated for this case, between selected probe pins. The impact of the modulation is clearly visible in the Transfer Entropy. The modulation leads to maxima in the Transfer Entropy at a specific time delay only in the right column of graphs, while the left column shows weak or no response to the modulation. This difference implies rotation in a specific direction. Similar to the previous case, the time delay is of the order of $2 - 3$ μs, and again the V-shape of the modulation is reflected by the temporal variation of the observed time delay.

Note that the Transfer Entropy between radially separated pins (middle row of Fig. 8) also shows uni-directional propagation, modulated by the external biasing, suggesting radially inward motion at similar speeds of the poloidal propagation. One

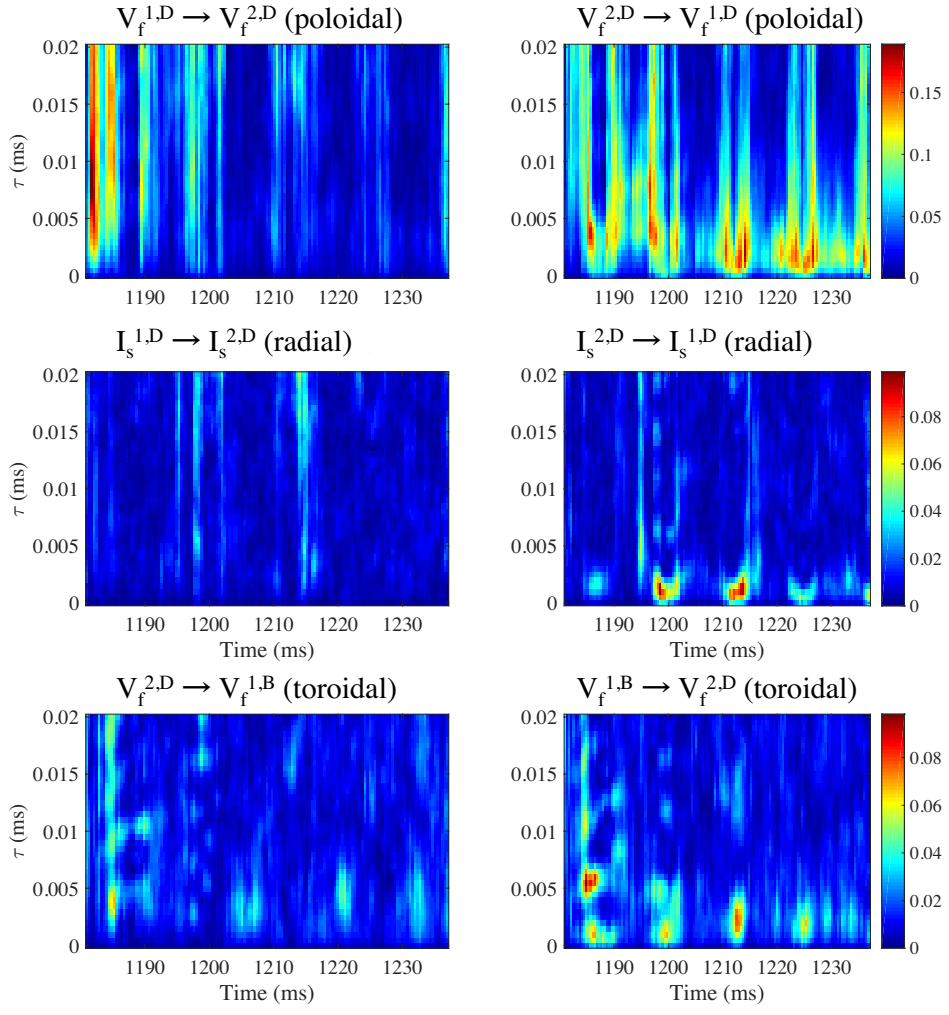

Figure 8. Transfer entropy (discharge 41373). Top: between two poloidally separated probe pins measuring V_f; Middle: between two radially separated probe pins measuring $I_{\rm sat}$; Bottom: between a reference pin (probe D) and a radial pin of probe B (the rake probe) measuring V_f.

may speculate that rather than a pure inward propagation, one is dealing with the radial projection of the poloidal propagation of elliptically shaped filaments, tilted at an angle with respect to the radial or poloidal directions - which would account for the similar propagation speed. Indeed, a tilted elliptical shape is what one would expect in the presence of an ambient sheared radial electric field (or, equivalently, an ambient sheared poloidal flow velocity) [13].

3.3. Radial and toroidal size of the filamentary structure

Fig. 8 (bottom row) shows the Transfer Entropy between a reference pin (probe D) and a selected pin from probe B. Again, propagation is visible in a specific direction, matching the externally imposed biasing (at $t \simeq 1200, 1213, 1225$ ms). This result indicates clearly that the filaments have a toroidal extension at least as long as the separation between the two probes (of the order of 5 m), which is consistent with earlier results based on the correlation [7].

The Transfer Entropy also shows a smaller reverse interaction occurring in the time intervals *between* modulation pulses (left panel of the figure, at times $t \simeq 1207, 1220, 1232$ ms). This is interesting: whereas during biasing, the plasma rotates such that information flows from probe B to probe D, when biasing is off, information flows from probe D to probe B (although weaker and somewhat slower). In section 4, we will propose an explanation for this phenomenon: in fact, the filamentary structure may be so long that it performs more than a single toroidal transit; again, this would be consistent with earlier work [7], in which parallel correlation lengths of up to about 50 m were deduced. This means that a single filamentary structure may cross a probe pin several times as it rotates poloidally. This effect can be seen in Fig. 8, in the bottom right panel, at time $t \simeq 1213$ ms: a small Transfer Entropy peak is seen at a lag of 0.013 ms, in addition to the large peak at a lag of 0.003 ms. Therefore, the structure seen in the left bottom panel does not actually indicate a flow reversal, but rather is the result from the repeated passage of a mode-like structure - even so, clearly this structure is not coherent, in view of the amplitude decay.

The data from the rake probe (probe B) can also be used to determine the radial extent of these filaments. Taking the same pin from probe D as reference ($V_f^{D,2}$), we calculate the Transfer Entropy between this pin and all pins of the rake probe. The result is shown in Fig. 9, after averaging the Transfer Entropy obtained in the time window $1210 < t < 1238$, considering only time lags $\Delta t < 0.01$ ms. Due to this averaging, which includes times at which no filaments are detected, the curve is not expected to fall to zero for large $|\Delta r|$. Consequently, we can determine its width by fitting a Gaussian with an offset ($N(0, \sigma^2) + C$, where $N(\mu, \sigma^2)$ is the normal Gaussian distribution centered at μ and with width σ, and C is a constant). This fit then reveals that the propagating filaments have a radial width of $2\sigma = 7 \pm 3$ mm, in a statistical sense.

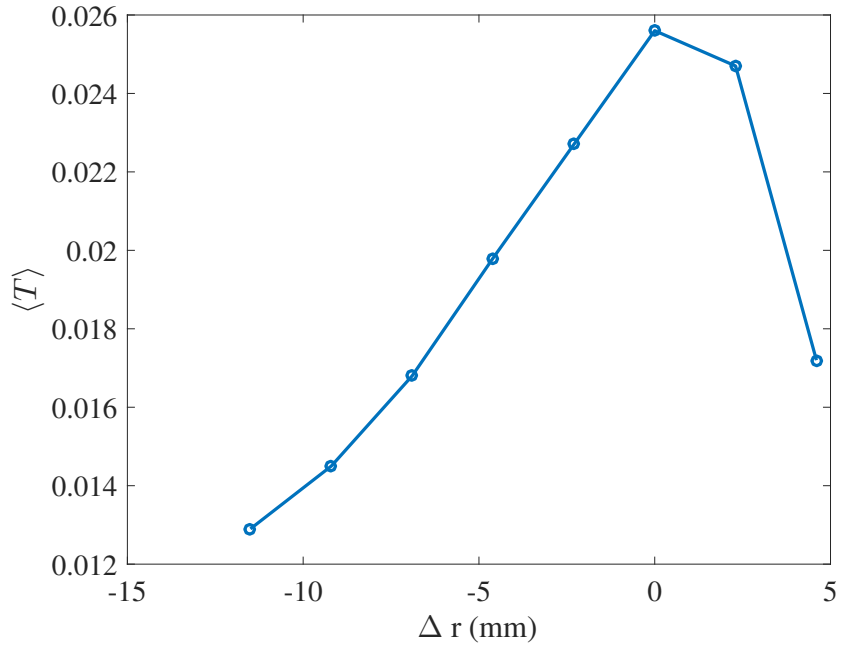

Figure 9. Mean Transfer Entropy between a reference pin (probe D) and the radial pins of probe B (the rake probe).

4. Resistive Magneto-HydroDynamic model

The purpose of the calculations presented here is to interpret the experimental observations presented in the previous sections. Using a resistive MHD model, we study plasma rotation by applying the Transfer Entropy method to electrostatic potential signals. Long structures (filaments) associated with vortices and aligned with the magnetic field can be observed [1]. These filaments inherit the periodicity of the magnetic field and evolve with the plasma itself. Therefore, as the plasma rotates, the filaments rotate as well.

In order to identify a filament we can measure the electrostatic potential at different toroidal locations in the plasma. The Transfer Entropy, a causality detection method, indicates whether a filament (a perturbation) has crossed our measuring points. Therefore, one can use the Transfer Entropy to detect the filaments on a given rational surface using two local signals at the same surface but at different toroidal and poloidal angles. In the present work, we use this technique to detect the presence of filaments, their periodicity, the plasma rotation along the surface and the width of the filaments.

The model used is a two-fluid resistive MHD turbulence model which has been used in the past to interpret some of the results from TJ-II experiments [14]. It is based on the Reduced MHD equations [15], the dominant instability being pressure gradient driven modes. The geometry of the system is a periodic cylinder (r, θ, ζ), where the averaged magnetic field line curvature is κ, r is the radial coordinate, a is the radius of the cylinder, θ is the poloidal angle and B_0 is the axial magnetic field. If the cylinder were bent into a torus, the toroidal angle would be $\zeta = z/R_0$, where z is the coordinate along the axis of the cylinder and R_0 is an effective major radius.

The set of dimensionless model equations is

$$\begin{aligned}
\frac{\partial \tilde{\psi}}{\partial t} &= \nabla_\parallel \Phi - S\bar{\omega}_{*e}\left(\frac{T_{eq}}{n_{eq}}\nabla_\parallel n + \nabla_\parallel T_e\right) + \eta \tilde{J}_z, \\
\frac{\partial \tilde{U}}{\partial t} &= -V_\perp \cdot \nabla U + S^2 \nabla_\parallel J_z - S^2 \frac{\beta_0}{2\varepsilon^2}\kappa\left(\frac{T_{eq}}{n_{eq}}\frac{1}{r}\frac{\partial \tilde{n}}{\partial \theta} + \frac{1}{r}\frac{\partial \tilde{T}_e}{\partial \theta}\right) + \mu \nabla_\perp^2 \tilde{U}, \\
\frac{\partial \tilde{n}}{\partial t} &= -V_\perp \cdot \nabla n + \frac{S}{\bar{\omega}_{ci}}\nabla_\parallel J_z + D_\perp \nabla_\perp^2 \tilde{n}, \\
\frac{\partial \tilde{T}_e}{\partial t} &= -V_\perp \cdot \nabla T_e + \frac{S}{\bar{\omega}_{ci}}\frac{T_{eq}}{n_{eq}}\nabla_\parallel J_z + \chi_\perp \nabla_\perp^2 \tilde{T}_e + \nabla_\parallel \left(\chi_\parallel \nabla_\parallel Te\right).
\end{aligned} \tag{2}$$

Here, ψ is the poloidal magnetic flux, $V_\perp$ is the perpendicular component of the velocity, U is the toroidal component of the vorticity, n is the density and T_e is the electron temperature. The tildes indicate fluctuations and the subindices "eq" indicate equilibrium profiles. $\tilde{U} = \nabla_\perp^2 \Phi / B_0$ where Φ is the electrostatic potential. $J_z = \nabla_\perp^2 \psi$ is the toroidal current and η is the resistivity. The viscosity coefficient is μ, $D_\perp$ is the perpendicular density diffusion and $\chi_\parallel$ ($\chi_\perp$) is the parallel (perpendicular) heat conductivity. β_0 is the ratio of the plasma pressure p and the magnetic pressure, $B_z^2/2\mu_0$, where μ_0 is the vacuum permeability. The resistive time is $\tau_R = \mu_0 a^2/\eta(0)$ where $\eta(0)$ is the resistivity at the magnetic axis. The Alfvén time is $\tau_A = R_0\sqrt{\mu_0 m_i n_i}/B_z$

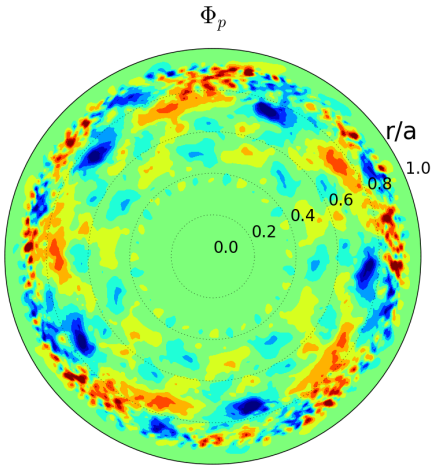

Figure 10. Perturbed electrostatic potential $\Phi_p = \Phi - \langle\Phi\rangle$ at some arbitrary time and toroidal angle.

where m_i and n_i are the ion mass and density, respectively. The Lundquist number is $S = \tau_R/\tau_A$. The inverse aspect ratio is $\varepsilon = a/R_0$. The normalized frequencies appearing in the equations are $\bar{\omega}_{*e} = \tau_A \omega_{*e}$, where $\omega_{*e} = T_e/\left(ea^2 B_z\right)$ is the electron diamagnetic frequency; and $\bar{\omega}_{ci} = \tau_A \omega_{ci}$, where $\omega_{ci} = m_i/\left(eB_z\right)$ is the ion cyclotron frequency.

In the simulations, $S = 2 \times 10^5$, $\beta_0 = 10^{-3}$, $\bar{\omega}_{*e} = 2 \times 10^{-4}$, $\bar{\omega}_{ci} = 500$. Lengths are normalized to the minor radius a and times to τ_R. A detailed explanation of the model can be found in Ref. [14]. The evolution equation of the averaged poloidal velocity $\langle V_\theta \rangle$ is derived by taking the flux surface average of the poloidal momentum balance equation. The resulting equation is

$$\frac{\partial \langle V_\theta \rangle}{\partial t} = -\frac{1}{r^2}\frac{\partial}{\partial r}\left(r^2 S_{r\theta}\right) - \hat{\mu}\langle V_\theta \rangle ,$$

where $S_{r\theta}$ is the non-diagonal $r\theta$ component of the Reynolds stress tensor which has two terms, an electrostatic and a magnetic component,

$$S_{r\theta} = \left\langle \tilde{V}_r \tilde{V}_\theta \right\rangle - S^2 \left\langle \tilde{B}_r \tilde{B}_\theta \right\rangle .$$

and $\langle\ \rangle$ denotes and average over the poloidal and toroidal angles.

We have used the rotational transform profile of configuration 100_44, as shown in Fig. 1. Figure 10 displays the perturbed electrostatic potential $\Phi_p = \Phi - \langle\Phi\rangle$ at some arbitrary time and toroidal angle. It has been obtained by self-consistently evolving the equations until a steady state is reached. The filamentary structure is revealed easily by highlighting the spatial points where the electrostatic potential $\Phi_p > 0.9\Phi_{p\ \max}$ (see Fig. 11) and bending the cylinder into a torus for visualization purposes.

The experiments reported above involved the use of Langmuir probes to measure the electric potential in the edge of the plasma, and relatively long time series could be obtained. A limitation of the experiments is that locations further inward (in the core) are not physically accessible. Contrasting with this, numerical simulations allow

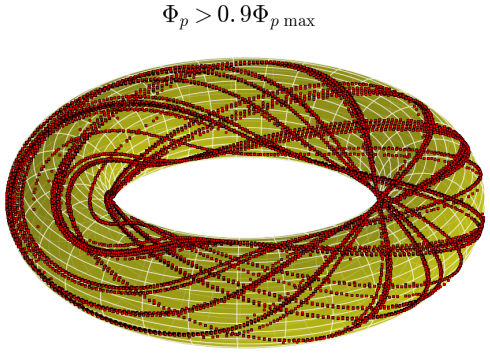

Figure 11. Filamentary structure of the electrostatic potential.

us to explore all desired radial and poloidal positions. In the present study, the length of the numerical time series we obtained is $0.1\tau_R$, which is enough time for more than one poloidal rotation of the plasma.

4.1. Filament length

Filaments can be very long structures. If one focuses only on the poloidal direction, filaments appear very close to each other. However, the connection length between two points in a filament can be very long. Figure 12 illustrates this idea. The diagonal shaded areas show the regions where the electrostatic potential is significantly positive ($\Phi_p > 0.1\Phi_{p\,\max}$) on a fixed radial surface and at a specific point in time (so white diagonal areas approximately correspond to regions where Φ_p is negative). The selected radial position is close to the location of the $n/m = 8/5$ rational surface ($r/a \approx 0.75$). In this work, we measure Φ_p at different locations in the plasma, imitating the experimental probes. There are 121 "probes", the first one is located at $\theta = 0$ and $\zeta = 0$ (red square). The other 120 are located at $\zeta = 180°$ (red horizontal line) and are separated by a poloidal distance $\Delta\theta \approx 2.3°$. The dashed diagonal line shows the path from the reference probe to the probe set along the filament structure. Therefore, even if our reference probe and the probes of the set are separated by $\Delta\zeta = 180°$, the shortest connection along the filament involves almost two toroidal rotations. Converting this length to meters using the values of R_0 and a for TJ-II, one obtains approximately 14.8 m, although the toroidal distance between probes (on *opposite sides* of the device, similar to Fig. 2) is only 4.7 meters.

The Transfer Entropy between the reference probe and the probe set will detect the filament structure only if the connection (path) that links them is not broken. But if the filament is broken in two or more pieces there may not exist a path between the probes and the Transfer Entropy method would not work. The behavior of broken filaments

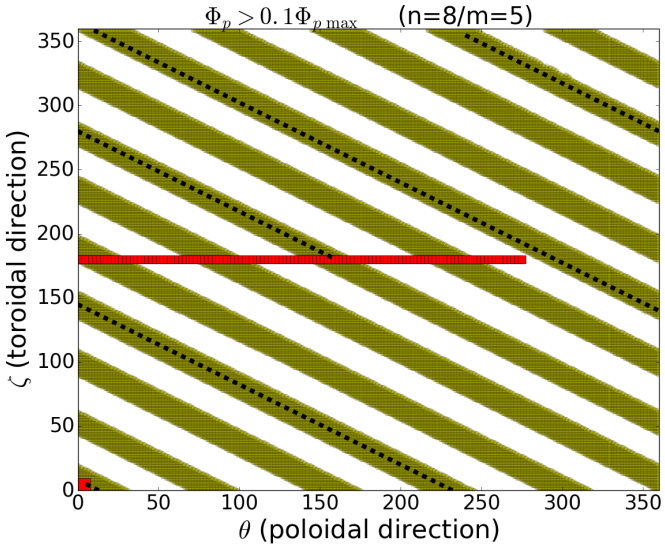

Figure 12. Positive electrostatic potential (shaded diagonal areas) at the fixed radial position $r/a = 0.75$, close to the 8/5 rational surface. The square at (0,0) is the reference probe and the horizontal line at $\zeta = 180°$ indicates the position of the probe set. The dashed diagonal line represents the shortest path between the reference point and one of the points in the probe set.

will be studied in a future work.

4.2. Periodicity of filaments

Using the set of synthetic measurements described above, the Transfer Entropy should be able to capture when a rotating filament, which crossed the reference probe also crosses the other set of probes on the other side of the cylinder, some time later.

The Transfer Entropy between the reference probe ($\zeta = 0$) and the probe set ($\zeta = 180°$) is calculated and represented in Fig. 13 for two different radial locations. In the upper figure, all signals are taken at $r/a = 0.75$ which is close to the location of the 8/5 rational surface. At that rational surface, the electrostatic potential has a poloidal periodicity $m = 5$, which means 5 maxima and 5 minima. That periodicity is observed in the upper plot in Fig. 13. At a given time lag, there are 5 regions (for a half poloidal section) where the Transfer Entropy is maximum. Therefore the Transfer Entropy is responding not only to the filament that crossed the reference probe, but to all filaments with the same periodicity. One might expect to obtain a high value of the Transfer Entropy when the filament that has passed the first probe reaches the other set of probes. However, the Transfer Entropy is observed to drop for increasing time lag. So probably, as the filament rotates, the perturbation itself is evolving and after some time the Transfer Entropy method cannot identify it.

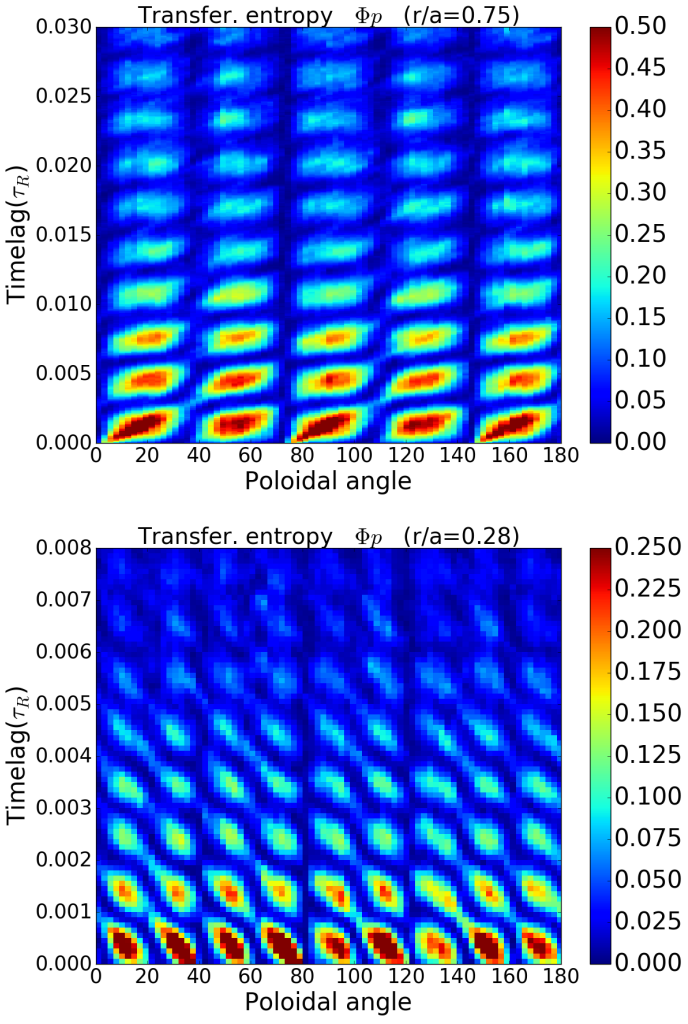

Figure 13. Transfer entropy between the reference probe ($\zeta = 0$) and the set of 120 probes ($\zeta = 180°$) placed at different poloidal angles. The top plot shows signals at $r/a = 0.75$ and the bottom plot at $r/a = 0.28$.

4.3. Poloidal velocity

Since the plasma is rotating, the perturbations of Φ_p are also rotating, which leads to a tilt of the roughly elliptical areas where the Transfer Entropy is high, visible in the upper plot in Fig. 13. This tilt is a consequence of the fact that the filament moves in the poloidal direction as time advances. The bottom plot of Fig. 13 displays a slope in the opposite direction (negative), due to the fact that the plasma rotations in the opposite direction at that radial position.

The angle of the tilt allows deducing the average angular velocity $\langle V_\theta \rangle$ of the perturbations of Φ_p at a given radial position from the Transfer Entropy shown in Fig. 13, as follows: $\langle V_\theta \rangle = \omega r = (\Delta\theta/\Delta\tau)r$, where $\Delta\theta$ and $\Delta\tau$ correspond to the x and y components of the angle of the tilted structures of Fig. 13.

The average polodial velocity can be also calculated from the numerical code. For

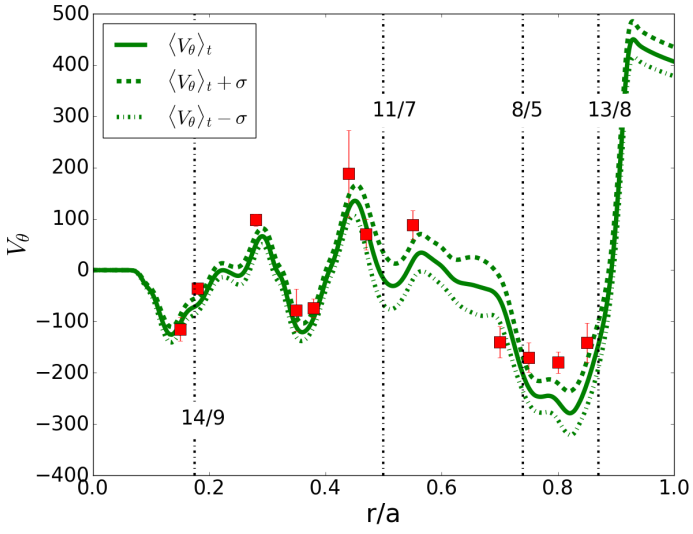

Figure 14. Poloidal velocity calculated directly from the simulation (solid line) with the corresponding standard deviation (dashed and dash-dotted lines) and from the Transfer Entropy method (dots). Main rational surfaces are indicated by the vertical dashed lines.

the results reported here, $\langle V_\theta \rangle$ varies only slightly in time. Figure 14 shows the average poloidal velocity calculated directly from the numerical code (solid line); the dashed and dash-dotted curves indicate one standard deviation, calculated from the temporal variation. The dots represent the poloidal velocity calculated using the Transfer Entropy method, as exemplified by Fig. 13. The Transfer Entropy method results are consistent with the actual poloidal velocity: the direction of the poloidal velocity is reproduced accurately, and the magnitude is generally close.

4.4. Radial width of the filaments

In the previous subsections, we studied the filamentary structure and rotation using synthetic probes distributed poloidally at a fixed radial position. Now, to study the radial extension of the filaments, we will define synthetic probes distributed radially.

For this purpose, we define one reference probe at $\theta = 0$, $\zeta = 0$ and $r/a = 0.75$, and 400 radial probes at $\theta = 46°$, $\zeta = 180°$, with a radial spacing of $\Delta r = 0.0025$. The Transfer Entropy between the reference probe and the radial probe set is shown in Fig. 15. Solid vertical lines show the location of main rationals. The dashed red vertical line indicates the radial position of reference signal which was chosen at the position of the 8/5 rational surface on purpose. Clearly, there is a region of high entropy associated with that rational surface. The radial width of that region is likely a good estimation of the filament width. With increasing time lag, Transfer Entropy maxima appear in a repetitive fashion, gradually decaying in amplitude. This effect is due the rotation of filaments associated with the rational surface, passing through the measuring point.

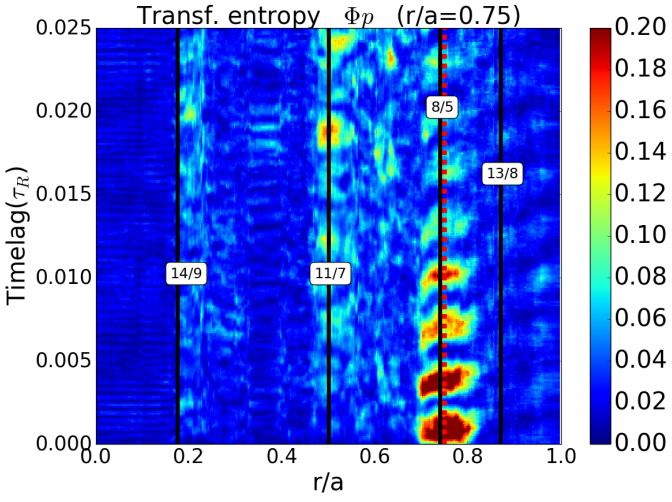

Figure 15. Transfer entropy between a reference probe at a fixed radial position $r/a = 0.75$ and a set of radial probes at a different angle. Black solid lines indicate main rationals. The red dashed line shows the position of the reference probe.

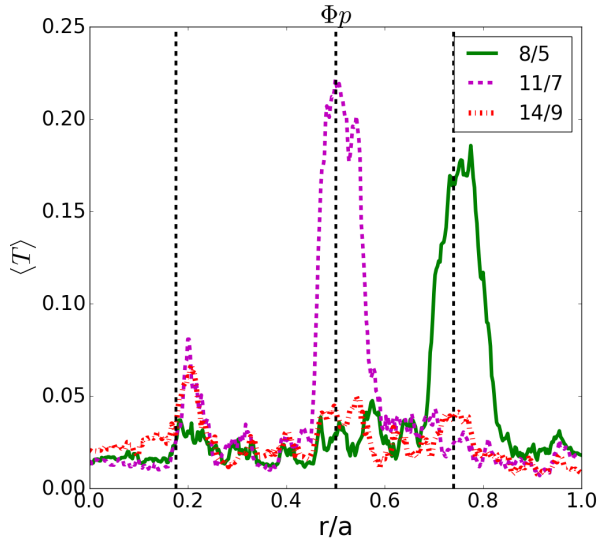

Figure 16. Mean Transfer Entropy between a reference probe at a fixed radial position and a set of radial probes at a different angle. The reference signals of the three curves are located at the rational surface, indicated by vertical dashed lines.

We now repeat the exercise, but setting the reference probe at three different major rational surfaces. Then we average the Transfer Entropy over $\tau \leq 0.0015$. The result is shown in Fig. 16. The three curves each show a peak centered at or near the actual rational surface (vertical lines). It appears these curves provide a good indication of the radial extent of the filaments. Probably, peaks are higher for the two outer rationals because they are more dominant.

5. Discussion and conclusions

In this work, we have used the Transfer Entropy in TJ-II plasmas with externally applied biasing to determine several characteristics of edge filaments. The Transfer Entropy calculated from spatially separated probe pins is insensitive to global (poloidally and toroidally symmetric) fluctuations such as Zonal Flows (ZFs). Zonal flows are known to arise both spontaneously [16] and during biasing [17] in TJ-II plasmas, and to give rise to enhanced Long Range Correlations (LRCs). Previous work has pointed out that such LRCs can also be generated by filamentary structures [7]. Nevertheless, in a situation with changing plasma conditions (a modification of the radial electric field due to a change of Neoclassical root or externally applied biasing), the enhancement of LRCs could confidently be ascribed to ZFs. The present study suggests a new method to distinguish LRCs due to ZFs and other sources (filaments): namely, by comparing results from standard correlation techniques (sensitive to LRCs due to both ZFs and filaments) and the Transfer Entropy (not sensitive to ZFs).

The radial width of the filaments was determined as 7 ± 3 mm in a given case. These results complement previous results [7], in which it was found that the size of the filamentary structures along the field lines is $L_{||} \simeq 40 - 50$ m (implying 4 to 5 toroidal turns), whereas the size of the structures perpendicular to the field lines (on the flux surface) is $L_{\perp} \simeq 7$ cm. Together, these data provide an experimental characterization of the three-dimensional structure of a typical filament in the TJ-II edge.

We have performed MHD simulations to corroborate these findings. The simulation data were analyzed by defining synthetic probes and applying the same analysis as was used to analyze the experimental data. Of course, in the simulation we could explore plasma regions that are not accessible by the probes. Data taken along the poloidal direction within a rational surface were used to elucidate the rotation of the filaments and to show how they pass through successive diagnostic locations. The Transfer Entropy captures the rotation of the filaments and allows calculating their rotation velocity. This deduced velocity was compared to the (known) poloidal velocity of the plasma and showed a relatively good agreement.

We also calculated the width of some filaments in the simulation using the Transfer Entropy technique. For this purpose, we used one fixed reference probe and a set of probes distributed radially at a different but fixed poloidal and toroidal angle. When the fixed reference probe was located at a rational surface, the Transfer Entropy showed a clear peak around that position. The deduced filament width (0.1 in units of $\rho = r/a$, or about 2 cm when translated to TJ-II) roughly agrees with the radial filament width reported in the experiments.

Acknowledgements

The authors would like to thank the TJ-II team for its continued support. Research sponsored in part by the Ministerio de Economía y Competitividad of Spain under

project Nrs. ENE2015-68265-P and ENE2015-68206-P. This work has been carried out within the framework of the EUROfusion Consortium and has received funding from the Euratom research and training programme 2014-2018 under grant agreement No 633053. The views and opinions expressed herein do not necessarily reflect those of the European Commission.

References

[1] B.A. Carreras, I. Llerena Rodríguez, and L. García. Topological structures of the resistive pressure gradient turbulence with averaged poloidal flow. *Nucl. Fusion*, 54:103005, 2014. doi:10.1088/0029-5515/54/10/103005.

[2] D.A. D'Ippolito, J.R. Myra, and S.J. Zweben. Convective transport by intermittent blob-filaments: Comparison of theory and experiment. *Phys. Plasmas*, 18:060501, 2011. doi:10.1063/1.3594609.

[3] F. Medina, M.A. Pedrosa, M.A. Ochando, L. Rodríguez, C. Hidalgo, A.L. Fraguas, B.A. Carreras, and the TJ-II Team. Filamentary current detection in stellarator plasmas. *Rev. Sci. Instrum.*, 72(1):471, 2001. doi:10.1063/1.1310579.

[4] D. Carralero, E. de la Cal, J.L. de Pablos, A. de Coninck, J.A. Alonso, C. Hidalgo, B.Ph. van Milligen, and M.A. Pedrosa. Turbulence studies by fast camera imaging experiments in the TJII stellarator. *J. Nucl. Mat.*, 390-391:457, 2009. doi:10.1016/j.jnucmat.2009.01.140.

[5] E. de la Cal, P. Semwal, A. Martin Aguilera, B. van Milligen, J.L. de Pablos, Z. Khan, and C. Hidalgo. Double imaging with an intensified visible fast camera to visualize the fine structure of turbulent coherent plasma structures (blobs) in TJ-II. *Plasma Phys. Control. Fusion*, 56:105003, 2014. doi:10.1088/0741-3335/56/10/105003.

[6] G. Kocsis, A. Alonso, C. Biedermann, G. Cseh, A. Dinklage, M. Jakubowski, R. König, M. Krychowiak, M. Otte, T. Sunn Pedersen, T. Szepesi, S. Zoletnik, and the W7-X Team. Investigation of edge filament dynamics in W7-X limiter plasmas. In *ECA*, volume 40A, page P4.003, 2016. URL: http://ocs.ciemat.es/EPS2016PAP/pdf/P4.003.pdf.

[7] B.Ph. van Milligen, A. Lopez Fraguas, M.A. Pedrosa, C. Hidalgo, A. Martin de Aguilera, and E. Ascasíbar. Parallel and perpendicular turbulence correlation length in the TJ-II stellarator. *Nucl. Fusion*, 53:093025, 2013. doi:10.1088/0029-5515/53/9/093025.

[8] T. Schreiber. Measuring information transfer. *Phys. Rev. Lett.*, 85(2):461, 2000. doi:10.1103/PhysRevLett.85.461.

[9] B.Ph. van Milligen, G. Birkenmeier, M. Ramisch, T. Estrada, C. Hidalgo, and A. Alonso. Causality detection and turbulence in fusion plasmas. *Nucl. Fusion*, 54:023011, 2014. doi:10.1088/0029-5515/54/2/023011.

[10] B.Ph. van Milligen, B.A. Carreras, L. García, A. Martin de Aguilera, C. Hidalgo, J.H. Nicolau, and the TJ-II Team. The causal relation between turbulent particle flux and density gradient. *Phys. Plasmas*, 23:072307, 2016. doi:10.1063/1.4958806.

[11] P.H. Diamond, S.-I. Itoh, K. Itoh, and T.S. Hahm. Zonal flows in plasma - a review. *Plasma Phys. Control. Fusion*, 47(5):R35, 2005. doi:10.1088/0741-3335/47/5/R01.

[12] A.V. Melnikov, C. Hidalgo, L.G. Eliseev, E. Ascasibar, A.A. Chmyga, K.S. Dyabilin, I.A. Krasilnikov, V.A. Krupin, L.I. Krupnik, S.M. Khrebtov, A.D. Komarov, A.S. Kozachek, D. López-Bruna, S.E. Lysenko, V.A. Mavrin, J.L. de Pablos, I. Pastor, S.V. Perfilov, M.A. Pedrosa, R.V. Shurygin, V.A. Vershkov, T-10 Team, and TJ-II Team. Plasma potential and turbulence dynamics in toroidal devices (survey of T-10 and TJ-II experiments). *Nucl. Fusion*, 51(8):083043, 2011. doi:10.1088/0029-5515/51/8/083043.

[13] R. Sánchez, D.E. Newman, J.-N. Leboeuf, and V.K. Decyk. Nature of turbulent transport across sheared zonal flows: insights from gyrokinetic simulations. *Plasma Phys. Control. Fusion*, 53:074018, 2011. doi:10.1088/0741-3335/53/7/074018.

[14] L. García, B.A. Carreras, V.E. Lynch, M.A. Pedrosa, and C. Hidalgo. Sheared flow amplification by vacuum magnetic islands in stellarator plasmas. *Phys. Plasmas*, 8(9):4111, 2001. doi:10.1063/1.1392996.

[15] H.R. Strauss. Nonlinear, threedimensional magnetohydrodynamics of noncircular tokamaks. *Phys. Fluids*, 19:134, 1976. doi:10.1063/1.861310.

[16] C. Hidalgo, M.A. Pedrosa, C. Silva, D. Carralero, E. Ascasíbar, B.A. Carreras, T. Estrada, F. Tabarés, D. Tafalla, J. Guasp, M. Liniers, A. López-Fraguas, B. van Milligen, and

M. Ochando. Multi-scale physics mechanisms and spontaneous edge transport bifurcations in fusion plasmas. *Europhys. Lett.*, 87:55002, 2009.

[17] M.A. Pedrosa, C. Silva, C. Hidalgo, B.A. Carreras, R.O. Orozco, D. Carralero, and the TJ-II Team. Evidence of long-distance correlation of fluctuations during edge transitions to improved-confinement regimes in the TJ-II stellarator. *Phys. Rev. Lett.*, 100:215003, 2008. doi:10.1103/PhysRevLett.100.215003.